Evolution of exchange interaction constants across magnetic phase transitions in the chromium spinel oxide $CdCr_2O_4$

Shojiro Kimura,* Yuya Sawada, Yasuo Narumi, and Kazuo Watanabe
Institute for Materials Research, Tohoku University, Katahira 2-1-1, Sendai 980-8577, Japan

Masayuki Hagiwara
Center for Advanced High Magnetic Field Science, Graduate School of Science, Osaka University, 1-1 Machikaneyama, Toyonaka 560-0043, Japan

Koichi Kindo
Institute for Solid State Physics, University of Tokyo, Kashiwa 277-8581, Japan

Hiroaki Ueda
Department of Chemistry, Graduate School of Science, Kyoto University, Kyoto 606-8502, Japan
(Received 1 May 2015; published 9 October 2015)

High field electron spin resonance (ESR) and magnetization measurements reveal the crucial role of the strong spin-lattice coupling to generate the peculiar phase transitions in the chromium spinel oxide $CdCr_2O_4$, which possesses a spin-driven Jahn-Teller transition and a field-induced 1/2-magnetization plateau state. From our analysis of the ESR modes and the spin wave dispersion, which was observed from the previous neutron scattering studies, these magnetic properties are shown to originate from the modifications of the exchange interactions due to the lattice distortions. The evaluated exchange constants are examined by the magnetoelastic theory proposed by Penc *et al*.

DOI: 10.1103/PhysRevB.92.144410 PACS number(s): 75.30.Kz, 75.60.Ej, 76.50.+g

I. INTRODUCTION

Over the years, phase transitions in geometrically frustrated spin systems have attracted attention because the spin degeneracy inherent in the ground state of the frustrated system strongly suppresses magnetic long-range order [1–3]. In most instances, a tiny perturbation, such as quantum fluctuations or couplings with the lattice or orbital degrees of freedom, leads to an unusual phase transition. One example of such phenomena is the "spin-driven Jahn-Teller effect" observed in the chromium spinel oxides ACr_2O_4 (A = Zn, Mg, Cd, and Hg) [4–10], where the spin-lattice coupling plays an essential role in relieving the geometrical frustration so that magnetic long-range order is realized. In ACr_2O_4, magnetic Cr^{3+} ions with spin $S = 3/2$ form a highly frustrated pyrochlore lattice, composed of a three-dimensional arrangement of corner sharing tetrahedra. Magnetic ordering in the chromium spinel oxides is first order, accompanied by spontaneous lattice distortion from cubic symmetry, $Fd\bar{3}m$ space group, to a lower symmetry. In other words, the geometrically frustrated magnetism on the pyrochlore lattice forces the crystal symmetry to be lowered, thereby lifting the degeneracy and inducing magnetic order. Recently, elastic deformations at magnetic ordering temperature, driven by geometrical magnetic frustration, have also been identified in triangular lattice antiferromagnets [11–15]. Interestingly, such a deformation in α-$NaMnO_2$ was reported to be inhomogeneous on the nanometer length scale [14].

A striking aspect of the pyrochlore antiferromagnets is that the vast ground-state degeneracy remains even in the presence of external magnetic fields [16]. In the chromium spinel oxides, this degeneracy generates a nontrivial magnetization plateau with half of the saturation value, hereafter referred to as the 1/2-plateau. More specifically, this plateau has been found in four kinds of chromium spinel oxides ACr_2O_4 with A = Zn, Mg, Cd, and Hg [17–25], and as shown in Fig. 1, the 1/2-plateau in $CdCr_2O_4$ appears at $H_{c1} \simeq 28.5$ T. The transition to the 1/2-plateau phase is very isotropic and is accompanied by a magnetostriction [17]. The powder neutron diffraction data for $HgCr_2O_4$, which possesses $H_{c1} \simeq 10$ T [18], provide insight about the 1/2-plateau phase and reveal a 16-sublattice ferrimagnetic structure, with cubic $P4_332$ symmetry, in which three up and one down spins occupy the vertices of each chromium tetrahedron [26]. Furthermore, it was also reported that the crystal structure in the 1/2-plateau region has the same distorted symmetry as the magnetic structure. This result indicates the spin-lattice coupling plays the main role in stabilizing the magnetization plateau. The subsequent neutron diffraction measurements in pulsed magnetic fields suggested that the magnetic structure in the plateau phase of $CdCr_2O_4$ is the same as the one identified for $HgCr_2O_4$ [27].

Theoretical studies also indicate spin-lattice coupling is important for the appearance of the stable 1/2-magnetization plateau in the chromium spinel oxides [16,28,29]. According to the theory by Penc *et al*., the spin-lattice coupling leads to an effective biquadratic interaction between spins, which favors collinear spin alignments [16,28]. From the calculations, which take into account the biquadratic interaction for classical spins on the pyrochlore lattice, magnetization curves consistent with the experimental results were obtained [16,28,30]. When the spin-lattice coupling works efficiently the atomic displacements due to the lattice deformation cause changes in exchange interactions. This mechanism is considered to be a

*shkimura@imr.tohoku.ac.jp

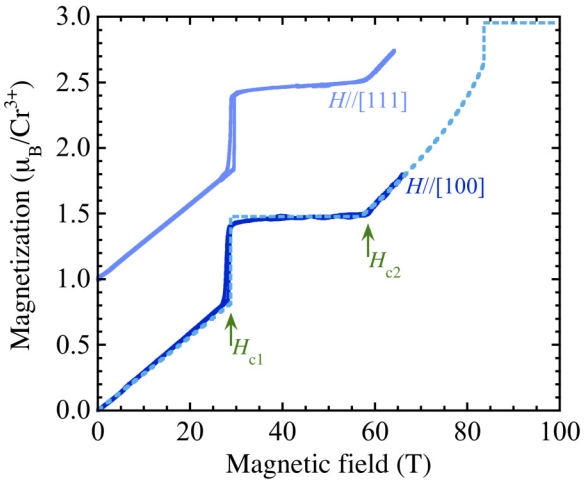

FIG. 1. (Color online) Magnetization curves of $CdCr_2O_4$ for $H \parallel [100]$ and [111]. The solid curves are the experimental results obtained at 1.3 K. The curve for $H \parallel [111]$ is shifted up by 1.0 μ_B/Cr^{3+} for clarity. The dashed curve is the result calculated using magnetoelastic theory.

reason why the robust magnetization plateau is stabilized in the chromium spinel oxides. In fact, our recent experiments showed the exchange interactions between Cr^{3+} spins are so significantly modified by the lattice distortion in the plateau phase of $HgCr_2O_4$ that the nearest-neighbor interactions become unequal to the extent the 1/2-plateau is stable [31].

Herein, for a more comprehensive understanding of the phase transitions in the chromium spinel oxides, the exchange interactions of $CdCr_2O_4$ in both zero and high magnetic fields have been investigated. In the case of $CdCr_2O_4$, for which good quality single crystals are available, the spin wave dispersion in zero field was obtained by neutron scattering measurements [32]. From our analysis of this spin wave excitation, the exchange interactions in the ordered phase in zero field are extracted. Furthermore, from the high field ESR and magnetization measurements, we evaluate the exchange interactions of $CdCr_2O_4$ in the plateau phase. With the analysis of these combined data sets, modifications of the exchange interactions are established for both the magnetic ordered phase and the field-induced transition to the 1/2-plateau phase. Furthermore, these changes of the exchange interactions are theoretically examined when incorporating the spin-lattice coupling, and the outcomes are compared to our previous results for $HgCr_2O_4$.

II. EXPERIMENTAL PROCEDURES

In our previous work, we reported the ESR and magnetization measurements of $CdCr_2O_4$, at 1.3 K and in magnetic fields up to 15 T, and suggested the spin structure varies from a helical structure, which was indicated from the neutron diffraction measurements at zero field, to a commensurate canted spin structure near 5.7 T [33]. Thus, for the present experiment, we focus on the results above 20 T. Specifically, high field ESR measurements of $CdCr_2O_4$ at 1.3 K were performed in pulsed magnetic fields up to about 53 T in the frequency region from 78 GHz to 1017 GHz utilizing Gunn oscillators and a far-infrared laser as light sources. For the observation of weak ESR signals, which are labeled as ω_{u1} and ω_{u2} in this paper, single crystals were used. On the other hand, the strong ESR signals ω_+ in high frequency region, observed by using the single crystals, show complex structures, which are probably due to interference effects. To avoid these issues, a small amount of the powder samples were used to measure the ESR signal ω_+. High field magnetization curves of $CdCr_2O_4$ up to 65 T were measured utilizing nondestructive pulse magnets by means of the induction method. Single crystals of $CdCr_2O_4$ were grown by a flux method. Powder samples were obtained by crushing the single crystals.

III. RESULTS AND ANALYSIS

A. Experimental results and evaluation of the exchange constants

Figure 1 shows the magnetization curves of $CdCr_2O_4$ at 1.3 K when $H \parallel [100]$ and [1 1 1], and these data are consistent with those reported previously [17,19,20,24]. The

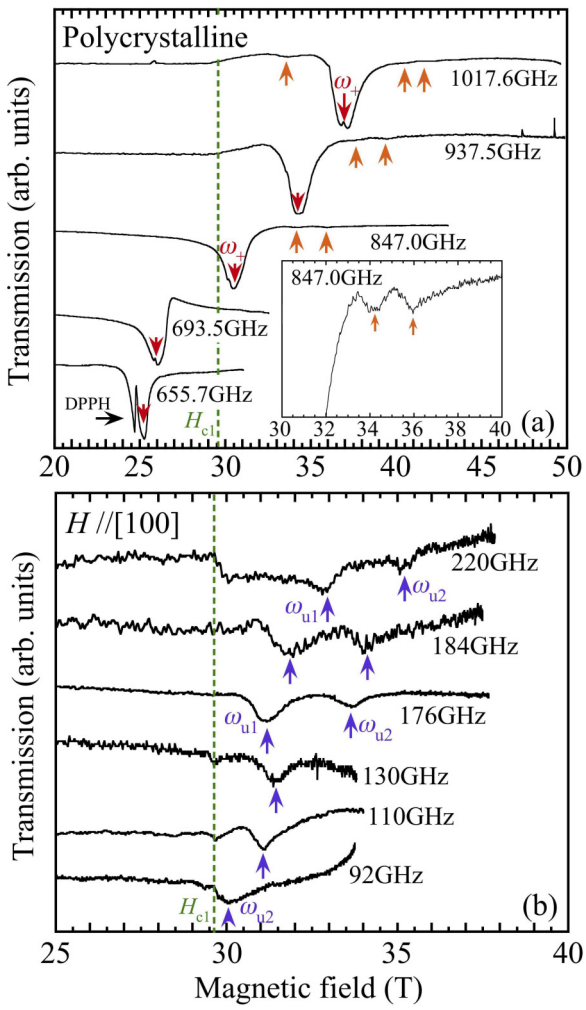

FIG. 2. (Color online) (a) Frequency dependence of ESR spectra in $CdCr_2O_4$, obtained at 1.3 K, in the frequency region from 655.7 GHz to 1016.7 GHz. The inset shows the extended ESR spectra at 847.0 GHz. (b) The ESR spectra in the frequency region from 92 GHz to 220 GHz. The vertical dashed line marks the transition field H_{c1}. These ESR spectra were observed when the field was increasing.

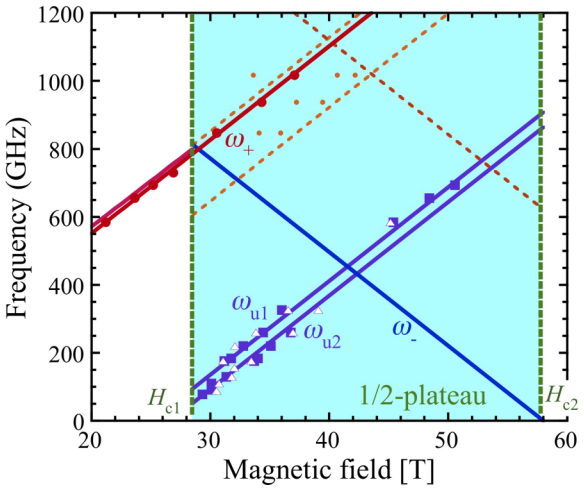

FIG. 3. (Color online) Frequency-field relation of the ESR resonance points in $CdCr_2O_4$. Closed circles are the ESR resonance points observed for the polycrystalline sample. Closed squares and open triangles are the data points acquired with a single crystal in magnetic fields applied along [100] and [111] axis, respectively. Solid and dashed lines designate the theoretical ESR modes. The two solid curves below H_{c1} are the theoretical antiferromagnetic resonance modes given from our previous analysis described in Ref. [28]. The vertical dashed lines mark the transition fields H_{c1} and H_{c2}.

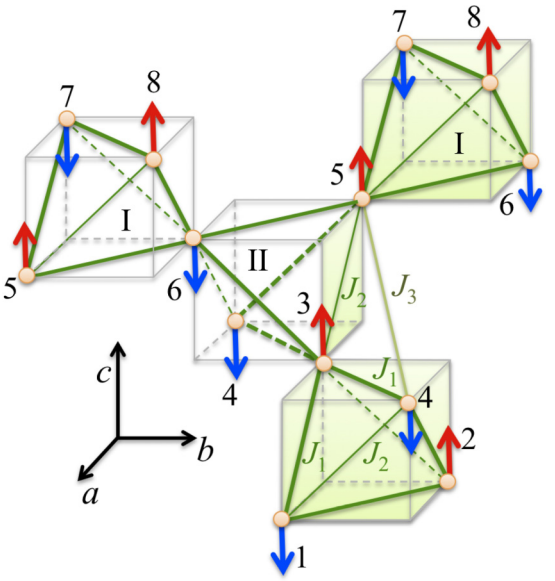

FIG. 4. (Color online) Assumed magnetic structure used for our analysis in zero magnetic field.

magnetization curves show a sudden jump into the 1/2-plateau phase at $H_{c1} \simeq 28.5$ T. The plateau phase ends at $H_{c2} \simeq 58$ T, and then the magnetization gradually increases above H_{c2}. It is noteworthy that our results show the transition fields H_{c1} and H_{c2} are both isotropic. Figures 2(a) and 2(b) show the ESR spectra of $CdCr_2O_4$ obtained at 1.3 K and in the frequency ranges from 655.7 GHz to 1017.6 GHz and from 92 GHz to 220 GHz, respectively. In the high frequency region, a strong ESR signal, ω_+, is observed at a paramagnetic resonance field with $g = 1.97$. In addition, several weak ESR signals appear near ω_+ in the 1/2-plateau phase above H_{c1}, as indicated by upward arrows in Fig. 2(a). In the low frequency region, two ESR signals, ω_{u1} and ω_{u2}, are observed in the 1/2-plateau phase as shown in Fig. 2(b). In addition, an anomaly of the baseline of the ESR spectra is seen at H_{c1}, and we speculate that this anomaly comes from a change of the dielectric constant due to the lattice transformation accompanying the transition to the plateau phase. The frequency-field relation of the observed ESR resonance points is shown in Fig. 3. All ESR modes obtained above H_{c1} have a positive slope with $g = 1.97$. In the following analysis, the exchange interactions in the ordered phase of $CdCr_2O_4$ in zero field are evaluated from the spin wave dispersion obtained from the previous neutron scattering measurements [32]. Then, the exchange interactions are evaluated in the plateau phase when using the analysis of our high field experimental results.

From the neutron diffraction measurements, the helical spin structure, characterized by an incommensurate wave vector $\boldsymbol{Q} = 2\pi(0,\delta,1)$ with $\delta \simeq 0.09$, was reported for the ordered state in $CdCr_2O_4$ in zero magnetic field [32]. The magnetic ordering of $CdCr_2O_4$ is accompanied by a lattice distortion from cubic to tetragonal symmetry with an elongated lattice ($a = b < c$) [32]. Recent theories demonstrated that the reported spin structure is compatible with a staggered lattice distortion with E_u symmetry [34,35]. More specifically, the pyrochlore lattice is composed of corner sharing of two kinds of tetrahedra, which are labeled as I and II in Fig. 4. The staggered lattice distortion, in which tetrahedra I and II are compressively distorted along the a and b axis, respectively, stabilizes the 8-sublattice collinear Néel order with $\boldsymbol{Q} = 2\pi(0,0,1)$, depicted in Fig. 4, through the change in the exchange interaction induced by the lattice distortion. In addition, the Dzyaloshinskii-Moriya (DM) interaction inherent in the pyrochrore lattice modulates the collinear structure to the helical one, and the experimentally observed (0, δ, 1) structure is stabilized by the third neighbor antiferromagnetic interaction J_3. In our previous study, we analyzed our ESR results below 5.7 T when assuming the helical structure is stabilized by competitive exchange interactions [33]. However, we now recognize the aforementioned theory, which takes the staggered distortion of the lattice into account, is a more valid interpretation of the ordered phase of $CdCr_2O_4$ in zero field. The spin wave dispersion, observed by the neutron scattering measurement, was explained by a theoretical magnon excitation from the ordered state with the helical spin structure characterized by $\boldsymbol{Q} = 2\pi(0,\delta,1)$ [35]. It was also suggested that the magnon excitation, numerically calculated by assuming 8-sublattice collinear ordering with exchange constants that are the same as those used in the calculation for the helical order, can reproduce the overall features of the experimentally observed spin wave dispersion when the DM interaction is neglected. Thus we analytically calculate the magnon excitation of the Néel ordered state with an 8-sublattice collinear spin structure, shown in Fig. 4, in terms of a classical spin wave theory. The details of the calculation are described in Appendix A. From the calculation, four kinds of the spin wave branches, each of which are doubly degenerate, are obtained. As mentioned in Ref. [27], due to the crystallographic domain, which is inevitably formed by the symmetry lowering from cubic to

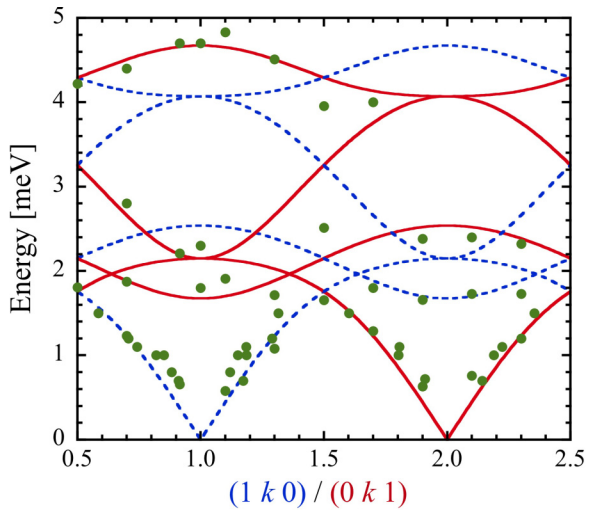

FIG. 5. (Color online) Spin wave dispersion for $CdCr_2O_4$ in zero magnetic field. Closed circles are the experimental results obtained from the previous neutron scattering measurement [32]. Dashed and solid curves are the theoretical results calculated for (1 k 0) and (0 k 1) directions, respectively.

tetragonal symmetry, the spin wave branches for the (1 k 0) and (0 k 1) directions are observed to be superimposed in the neutron scattering measurement. By accounting for this superposition, the experimental spin wave dispersion can be explained by the theoretical calculation, as shown in Fig. 5. The exchange constants, evaluated by this calculation, are $J_1 = 9.04$ K, $J_2 = 5.8$ K, and $J_3 = 1.05$ K. Here, J_1 and J_2 are the nearest-neighbor interactions between spins with antiparallel and parallel alignment, respectively. The second nearest-neighbor interaction is neglected in our analysis, because the previous first-principles *ab initio* calculations indicated it is much weaker than the third nearest-neighbor one, J_3 [34,36], and we assume J_3 remains intact through the lattice distortion. We recently reported the optical absorption arising from the exciton-magnon excitation in the infrared region also agrees with our spin wave calculation [37]. The zero field gaps, estimated from our previous ESR study [33], almost coincide with the calculated magnon energies at the magnetic zone center [1 1 0] or [0 1 1], except for the lowest gap. The finite energy of the lowest gap, observed in the experiments, is due to the small DM interaction or singe-ion anisotropy, which was neglected in our spin wave calculation. From our ESR measurement, the lowest gap was estimated to be 0.61 meV [33], which is consistent with the experimental spin wave dispersion. If one assumes that this lowest energy gap E_g comes from single-ion anisotropy, E_g is given as $E_g = 4S\sqrt{J_1 D}$, where D is a single-ion anisotropy constant. From this equation, D is evaluated to be $D/k_B = 0.16$ K, indicating the very isotropic nature of $CdCr_2O_4$.

Next, by analyzing our high field experimental results, we evaluate the exchange interactions in the 1/2-plateau phase. Different from the previous results in $HgCr_2O_4$ [31], the ω_u mode in $CdCr_2O_4$ splits into the two branches ω_{u1} and ω_{u2}, and no ω_- mode is observed. The ω_{u1} and ω_{u2}, observed for $H \parallel [100]$ and $H \parallel [111]$, almost coincide with each other as shown in Fig. 3. Therefore, the splitting between ω_{u1} and ω_{u2} is not due to a magnetic anisotropy. In order to analyze the observed ESR modes, we solve the resonance conditions for a 16-sublattice ferrimagnetic structure with the $P4_332$ symmetry while neglecting any small magnetic anisotropy. Details of the calculation are described in Appendix B. Our calculation shows the splitting of the ω_u modes can be reproduced by taking the third nearest-neighbor interaction J_3 into account. By introducing J_3, the ω_u mode with fivefold degeneracy, as calculated from the 16-sublattice ferrimagnetic structure, splits into the two branches ω_{u1} and ω_{u2}, which have three- and twofold degeneracy, respectively. For the analysis, we assume the exchange interaction J_1 is different from J_2, which is the nearest-neighbor interaction between the spins with parallel alignment, because of the lattice distortion with $P4_332$ symmetry, while the third nearest-neighbor interaction, $J_3/k_B = 1.05$ K, is held at its value in zero field. Next, the values of J_1 and J_2 are evaluated so as to reproduce ω_{u1}, ω_{u2}, and $H_{c2} = 58.0$ T, at which the ω_- mode becomes soft. The calculated ESR modes are shown in Fig. 3. Other than the ω_+, ω_-, ω_{u1}, and ω_{u2} modes, three kinds of the triply degenerate ESR modes, which are shown by dashed lines in Fig. 3, are derived from the 16-sublattice model. The weak signals observed near ω_+ probably come from these ESR modes. It should be mentioned that these weak ESR signals are not due to the splitting of ω_+ mode by the magnetic anisotropy, because the deviation of the resonance field of the ω_+ mode from the paramagnetic resonance line is estimated to be about $H_A \sim 2SD/g\mu_B \sim 0.36$ T, whereas the deviations of the weak ESR signals from the paramagnetic resonance field are more than 3 T. For a better reproduction of the ESR modes from these weak signals, we should take into account the second nearest-neighbor exchange interaction, which is neglected in this analysis.

From our analysis in the 1/2-plateau phase, the evaluated exchange constants are $J_1/k_B = 10.7$ K and $J_2/k_B = 6.08$ K. In the case of the 4-sublattice ferrimagnetic structure, in which all the tetrahedra are distorted in the same direction with the $R\bar{3}m$ symmetry, the ω_{u1} and ω_{u2} modes are degenerate, and no ESR modes other than ω_+, ω_-, and ω_u are derived from the calculation. It should be mentioned that the magnetic dipole transition for the ESR modes other than ω_+ and ω_- are forbidden in principle because the precession motion of the transverse components against the external magnetic field of each sublattice cancel each other. We suspect the electric dipole transition is the origin of the finite signal intensity of these forbidden ESR modes. In the 1/2-plateau phase, the lattice distortion with $P4_332$ symmetry breaks the inversion symmetry on the Cr^{3+} sites. In such a case, the Cr^{3+} spin can induce electric polarization via a spin-dependent metal-ligand hybridization [38–40], and consequently the magnon excitation possibly causes some oscillation of the electric dipole moment, which couples to the electric component of electromagnetic wave as in the case of $Ba_2CoGe_2O_7$ [39–41]. On the other hand, we could not find the ESR signal from the ω_- mode, although we measured the ESR spectra in magnetic fields of up to 53 T in the frequency region above 584 GHz. The inability to experimentally detect the ω_- mode in $CdCr_2O_4$ is considered to be due to its weak signal intensity, which results from its larger exchange interaction compared to the one in $HgCr_2O_4$. As mentioned in Ref. [26], if the small J_3

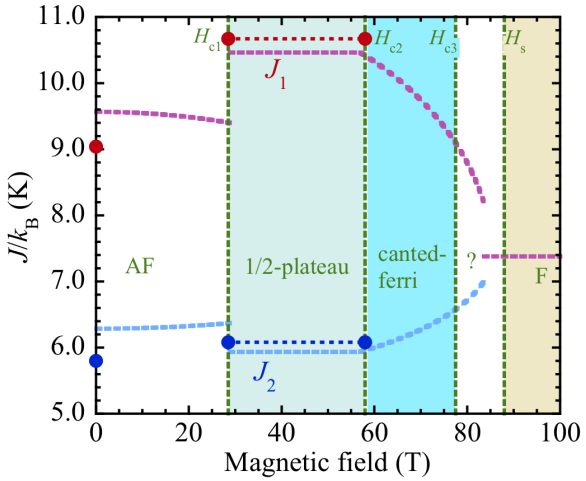

FIG. 6. (Color online) Exchange constants of the nearest-neighbor interactions in $CdCr_2O_4$. Closed circles are those evaluated from the analysis of the experimental results. Dashed curves are the results of the calculation based on the magnetoelastic theory. Vertical dashed lines are H_{c1}, H_{c2}, H_{c3}, and H_s.

is neglected, the ratio of the intensity of ω_- to that of ω_+ is roughly $|D/2J_1|^2$. Thus a large J_1 in $CdCr_2O_4$ results in a weak signal of ω_-. By using $D/k_B = 0.16$ K and $J_1/k_B = 10.7$ K, this value is evaluated to be $|D/2J_1|^2 \sim 5.6 \times 10^{-4}$, indicating that ω_- is hardly observable in our ESR system. The exchange constants J_1 and J_2 evaluated from our analysis are plotted in Fig. 6. Our analysis suggests the large inequality among the nearest-neighbor exchange interactions is caused by the lattice distortion, and a modification in the exchange constants occurs due to the field-induced transition to the 1/2-plateau phase. In the next subsection, the exchange constants evaluated from the above analysis and the magnetization curve in $CdCr_2O_4$ are examined by a theory that takes into account the spin-lattice coupling.

B. Analysis within the frames of the magnetoelastic theory

As described in Appendix C, according to the magnetoelastic theory proposed by Penc *et al.* [16,28], an effective Hamiltonian for a single tetrahedron embedded on the pyrochlore lattice is given as

$$\mathcal{H}_{\rm eff} = 2J\left(\sqrt{6}\Lambda_{A_1} - b_{A_1}\Lambda_{A_1}^2 - b_E\Lambda_E^2 - b_{T_2}\Lambda_{T_2}^2\right) - 4HM, \tag{1}$$

where J is the exchange constant when the system has no spin correlation, Λ_R's are functions expressed by scalar products of neighboring spins, as shown in Appendix C, and b_R is given as

$$b_R = J{\alpha_R}^2/K_R. \tag{2}$$

Here, the subscripts $R = A_1$, E, and T_2 represent the normal modes of vibration in a tetrahedron with a T_d symmetry [9,10,16,28]. Specifically, the A_1 mode uniformly stretches or contracts the tetrahedron, the E modes cause tetragonal and orthorhombic distortions, and the T_2 modes equally stretch and contract two opposing bonds. In Eq. (2), α_R is the strength of the spin lattice coupling and K_R is the elastic coupling constant for R ($R = A_1$, E, or T_2) mode. Penc *et al.* mentioned that if J, b_{A_1}, b_E, and b_{T_2} are determined, then the magnetic structure of the classical ground state can be uniquely determined at arbitrary strength of the magnetic field by minimizing Eq. (1), when one restricts the analysis to the 4-sublattice model with crystal momentum $q = 0$ [16]. From this resulting magnetic structure, the magnetization per site, $M = g\mu_B(S_1^z + S_2^z + S_3^z + S_4^z)/4$, is obtained. Moreover, from this theory the change in the exchange interaction during the magnetization process can also be calculated, as described in our previous paper [42]. By substituting Eq. (2) to Eq. (1), the exchange interactions $J_{i,j}$ between the nearest-neighbor spins $\boldsymbol{S}_i$ and $\boldsymbol{S}_j$ are derived as

$$J_{1,2} = J\left\{1 - \frac{2b_{A_1}}{\sqrt{6}}\Lambda_{A_1} - \frac{2b_E}{\sqrt{3}}\Lambda_{E,1} + \frac{2b_{T_2}}{\sqrt{2}}\Lambda_{T_2,3}\right\}, \tag{3}$$

$$J_{1,3} = J\left\{1 - \frac{2b_{A_1}}{\sqrt{6}}\Lambda_{A_1} + \frac{2b_E}{\sqrt{3}}\Lambda_{E,1} - b_E\Lambda_{E,2} + \frac{2b_{T_2}}{\sqrt{2}}\Lambda_{T_2,3}\right\}, \tag{4}$$

$$J_{1,4} = J\left\{1 - \frac{2b_{A_1}}{\sqrt{6}}\Lambda_{A_1} + \frac{b_E}{\sqrt{3}}\Lambda_{E,1} + b_E\Lambda_{E,2} + \frac{2b_{T_2}}{\sqrt{2}}\Lambda_{T_2,1}\right\}, \tag{5}$$

$$J_{2,3} = J\left\{1 - \frac{2b_{A_1}}{\sqrt{6}}\Lambda_{A_1} + \frac{b_E}{\sqrt{3}}\Lambda_{E,1} + b_E\Lambda_{E,2} - \frac{2b_{T_2}}{\sqrt{2}}\Lambda_{T_2,1}\right\}, \tag{6}$$

$$J_{2,4} = J\left\{1 - \frac{2b_{A_1}}{\sqrt{6}}\Lambda_{A_1} + \frac{b_E}{\sqrt{3}}\Lambda_{E,1} - b_E\Lambda_{E,2} - \frac{2b_{T_2}}{\sqrt{2}}\Lambda_{T_2,2}\right\}, \tag{7}$$

$$J_{3,4} = J\left\{1 - \frac{2b_{A_1}}{\sqrt{6}}\Lambda_{A_1} - \frac{2b_E}{\sqrt{3}}\Lambda_{E,1} - \frac{2b_{T_2}}{\sqrt{2}}\Lambda_{T_2,2}\right\}. \tag{8}$$

Importantly, these equations suggest the exchange interactions $J_{i,j}$ depend on scalar products of neighboring spins, which are determined by the magnetic structure. Therefore, a modification in the magnetic structure causes the variation of the exchange interaction, as indicated by our experiments.

The dashed curves in Figs. 1 and 6 are theoretical results, calculated based on the above magnetoelastic theory. The parameters used for the calculations are $J = 8.2$ K, $b_{A_1}S^2 = 0.05$, $b_E S^2 = 0.1$, $b_{T_2}S^2 = 0.14$, $g = 1.97$, and $J_3 = 1.05$ K. The calculated values of J_1 and J_2 in Fig. 6 correspond to $J_{1,3}$ and $J_{3,4}$, respectively. For $H < H_{c1}$, we assume an 8-sublattice Néel-type magnetic structure, in which the two up and two down spins on a tetrahedron shown in Fig. 4 cant towards the external field. In the 1/2-plateau phase, the 16-sublattice ferrimagnetic structure with $P4_332$ symmetry is assumed. For the 8-sublattice structure, the classical energy, calculated from Eq. (1), is the same for the each tetrahedral unit. In other words, the energies of the tetrahedra composed of $\boldsymbol{S}_1$, $\boldsymbol{S}_2$, $\boldsymbol{S}_3$, and $\boldsymbol{S}_4$ and of $\boldsymbol{S}_5$, $\boldsymbol{S}_6$, $\boldsymbol{S}_7$, and $\boldsymbol{S}_8$, shown in Fig. 4, are identical. A similar situation also applies to the 16-sublattice ferrimagnetic structure, where four kinds of tetrahedral units are included. In addition to the Hamiltonian in Eq. (1), J_3 is taken into account as a molecular field for the calculation of

TABLE I. Parameters of $CdCr_2O_4$ and $HgCr_2O_4$ (from Refs. [26,37]).

Sample	J_1/J_2	$(H_{c3} - H_{c1})/H_s$	$b_{A_1}S^2$	$b_E S^2$	$b_{T_2}S^2$	J/k_B	J_3/k_B
$CdCr_2O_4$	1.8	0.53	0.05	0.1	0.14	8.2	1.05
$HgCr_2O_4$	2.4	0.67	0.05	0.16	0.21	4.25	

the classical energy. The transition field H_{c1} is calculated as a field at which the ferrimagnetic phase becomes more stable than the Néel-type ordered phase. Then, the ferrimagnetic phase changes to the canted ferrimagnetic phase, in which the spins are smoothly canted from the collinear structure at H_{c2}, and finally the saturation of the magnetization is achieved. The calculated results agree reasonably well with the experimental results for both the magnetization curve and the exchange constants, as shown in Figs. 1 and 6. The theoretical curves in Fig. 6 indicate the difference between the exchange constants J_1 and J_2 gradually diminishes as the field is increased above H_{c2}. Such behavior, which comes from a gradual release of the lattice distortion, was experimentally suggested in $HgCr_2O_4$ [33]. The largest value of b_{T_2} among collection of b_R's, which causes the larger inequality between J_1 and J_2 in the 1/2-plateau phase than for $H < H_{c1}$ region, indicates the nearest-neighbor exchange interaction in $CdCr_2O_4$ is susceptible to a T_2-type lattice distortion. This result is similar to the case of $HgCr_2O_4$ [33], and the values of the parameters for $CdCr_2O_4$ and $HgCr_2O_4$ [33,42] are shown in Table I. The ratio J_1/J_2 in the 1/2-plateau phase, tabulated in Table I, indicates the relative change in the nearest-neighbor exchange interaction due to the lattice distortion for $HgCr_2O_4$ is larger than that for $CdCr_2O_4$. This outcome is consistent with the experimental result that the 3:1 magnetic structure in $HgCr_2O_4$ is relatively more stable than that in $CdCr_2O_4$, as indicated from the larger value of $(H_{c3} - H_{c1})/H_s$ for $HgCr_2O_4$. Here, H_{c3} is the magnetic field at which the canted ferrimagnetic phase ends, and H_s is the field where the transition to the fully polarized phase experimentally occurs [24,31]. In the theoretical calculation, the larger change in the nearest-neighbor exchange interaction requires larger b_E and b_{T_2} for $HgCr_2O_4$. As given in Eq. (2), b_R depends on the ratio of the spin lattice coupling constant α_R and the elastic coupling constant K_R. Therefore, our analysis indicates $HgCr_2O_4$ possesses a stronger spin-lattice coupling or softer crystal lattice than $CdCr_2O_4$. In addition, our study shows that magnetoelastic theory works well to reproduce the overall features of the high field experimental results in both $CdCr_2O_4$ and $HgCr_2O_4$.

However, the classical calculation based on this theory cannot explain the unexpected phase prior to the saturation of the magnetization, indicated from the experiments [21–24,31,42–44]. Our classical calculations based on the magnetoelastic theory suggest a jump of the magnetization due to the first order transition from the 3:1 canted phase to the fully polarized phase. On the other hand, the magnetization curve experimentally observed in $CdCr_2O_4$ only shows a kink at H_{c3}, where the 3:1 canted phase is considered to end, followed by a gradual increase up to the saturation field H_s, suggesting existence of another phase between these two phases [24]. This behavior is similar to that observed in $HgCr_2O_4$ [31,42], and such an unexpected phase was also reported for $ZnCr_2O_4$ from experiments in ultrahigh magnetic fields [22,23]. As a candidate of this unexpected phase, a spin nematic state was recently discussed [24]. It has been conjectured that a quantum condensed phase of two magnon bound pairs, which results in the spin nematic ordered state, can be stable near the saturation field in frustrated magnets [45–48]. A new magnetic phase, recently found near the saturation field of the frustrated $S = 1/2$ chain compound $LiCuVO_4$, was proposed to be such a spin nematic state [49]. For a deeper understanding of the unexpected phase in ACr_2O_4, a more detailed theoretical treatment, which takes into account quantum effects, is desired.

IV. CONCLUSION

High field ESR and magnetization measurements of the chromium spinel oxide $CdCr_2O_4$ were performed. From the analyses of the spin wave dispersion and our high field experimental results, we succeeded in evaluating the exchange constants in the ordered phase in zero magnetic field and those in the 1/2-plateau phase. The analyses showed the exchange interaction values become unequal between the nearest-neighbor spins with parallel and antiparallel alignments. This behavior arises from the spin Jahn-Teller transition that stabilizes the ordered magnetic structure. The difference among the nearest-neighbor exchange constants in the 1/2-plateau phase is larger than that in the ordered phase in zero field. This result indicates the spin system couples more strongly with the T_2-type vibration mode. By comparing with our previous results, it turned out that relative change in the exchange constants of $HgCr_2O_4$ is larger than that of $CdCr_2O_4$. We showed that the magnetoelastic theory agrees well with the high field experimental results in both $HgCr_2O_4$ and $CdCr_2O_4$, except for the behaviors just below the saturation fields.

ACKNOWLEDGMENTS

S.K. is grateful to Dr. M. Matsuda and Dr. J.-H. Chung for providing us with their neutron data, and also thanks to Professor Mark W. Meisel and Dr. K. Penc for their valuable comments. This work was partly supported by Grants-in-Aid for Scientific Research (No. 24340073 and No. 26620055) from MEXT Japan.

APPENDIX A

The spin wave frequencies are obtained by solving the equation of motion, which is expressed as follows:

$$\hbar(\partial \boldsymbol{S}_l(\boldsymbol{r}_i)/\partial t) = [\boldsymbol{S}_l(\boldsymbol{r}_i) \times \boldsymbol{H}(\boldsymbol{r}_i)], \tag{A1}$$

where $\boldsymbol{S}_l(\boldsymbol{r}_i)$ is a spin on the lth sublattice located at $\boldsymbol{r}_i$, $\boldsymbol{H}(\boldsymbol{r}_i)$ is an effective field acting on the $\boldsymbol{S}_l(\boldsymbol{r}_i)$, which is derived from differentiation of the assumed Hamiltonian $\boldsymbol{H}(\boldsymbol{r}_i) = \partial\mathcal{H}/\partial\boldsymbol{S}_l(\boldsymbol{r}_i)$. Here, $\mathcal{H}$ expresses Heisenberg exchange interactions between the nearest- and the third nearest-neighbor spins on the pyrochlore lattice. $\boldsymbol{r}_i$ is placed at the pyrochlore lattice with no distortion, and the lattice constants are defined as unity. The equilibrium directions of the spins are defined to be parallel

or antiparallel to the z axis. Assuming precession motion for the xy components, the following equations for the spin on the sublattice 1–4 are obtained:

$$\begin{aligned}\hbar\omega\Delta S_1 =& 2S(2J_1 - J_2 + 2J_3)\Delta S_1 + SJ_1\left\{e^{i(k_x-k_y)/4}\Delta S_2 + e^{i(-k_x+k_y)/4}\Delta S_2 + e^{i(-k_x+k_z)/4}\Delta S_3 + e^{i(-k_y-k_z)/4}\Delta S_8\right\}\\ &+ SJ_2\left\{e^{i(k_y+k_z)/4}\Delta S_4 + e^{i(k_x-k_z)/4}\Delta S_7\right\} + 2SJ_3\left\{\cos\left((k_x+k_y)/2\right) + \cos\left((k_x-k_y)/2\right)\right\}\Delta S_1\\ &+ 2SJ_3\left\{\cos\left((k_y+k_z)/2\right) + \cos\left((k_y-k_z)/2\right) + \cos\left((k_x+k_z)/2\right) + \cos\left((k_x-k_z)/2\right)\right\}\Delta S_5,\end{aligned} \tag{A2}$$

$$\begin{aligned}\hbar\omega\Delta S_2 =& -2S(2J_1 - J_2 + 2J_3)\Delta S_2 - SJ_1\left\{e^{i(k_x-k_y)/4}\Delta S_1 + e^{i(-k_x+k_y)/4}\Delta S_1 + e^{i(k_x+k_z)/4}\Delta S_4 + e^{i(k_y-k_z)/4}\Delta S_7\right\}\\ &- SJ_2\left\{e^{i(-k_y+k_z)/4}\Delta S_3 + e^{i(-k_x-k_z)/4}\Delta S_8\right\} - 2SJ_3\left\{\cos\left((k_x+k_y)/2\right) + \cos\left((k_x-k_y)/2\right)\right\}\Delta S_2\\ &- 2SJ_3\left\{\cos\left((k_y+k_z)/2\right) + \cos\left((k_y-k_z)/2\right) + \cos\left((k_x+k_z)/2\right) + \cos\left((k_x-k_z)/2\right)\right\}\Delta S_6,\end{aligned} \tag{A3}$$

$$\begin{aligned}\hbar\omega\Delta S_3 =& -2S(2J_1 - J_2 + 2J_3)\Delta S_3 - SJ_1\left\{e^{i(k_x-k_z)/4}\Delta S_1 + e^{i(k_x+k_y)/4}\Delta S_4 + e^{i(-k_x-k_y)/4}\Delta S_4 + e^{i(-k_y+k_z)/4}\Delta S_6\right\}\\ &- SJ_2\left\{e^{i(k_y-k_z)/4}\Delta S_2 + e^{i(-k_x+k_z)/4}\Delta S_5\right\} - 2SJ_3\left\{\cos\left((k_x+k_y)/2\right) + \cos\left((k_x-k_y)/2\right)\right\}\Delta S_3\\ &- 2SJ_3\left\{\cos\left((k_y+k_z)/2\right) + \cos\left((k_y-k_z)/2\right) + \cos\left((k_x+k_z)/2\right) + \cos\left((k_x-k_z)/2\right)\right\}\Delta S_7,\end{aligned} \tag{A4}$$

$$\begin{aligned}\hbar\omega\Delta S_4 =& 2S(2J_1 - J_2 + 2J_3)\Delta S_4 + SJ_1\left\{e^{i(-k_x-k_z)/4}\Delta S_2 + e^{i(k_x+k_y)/4}\Delta S_3 + e^{i(-k_x-k_y)/4}\Delta S_3 + e^{i(k_y+k_z)/4}\Delta S_5\right\}\\ &+ SJ_2\left\{e^{i(-k_y-k_z)/4}\Delta S_1 + e^{i(k_x+k_z)/4}\Delta S_6\right\} + 2SJ_3\left\{\cos\left((k_x+k_y)/2\right) + \cos\left((k_x-k_y)/2\right)\right\}\Delta S_4\\ &+ 2SJ_3\left\{\cos\left((k_y+k_z)/2\right) + \cos\left((k_y-k_z)/2\right) + \cos\left((k_x+k_z)/2\right) + \cos\left((k_x-k_z)/2\right)\right\}\Delta S_8.\end{aligned} \tag{A5}$$

Here, ΔS_i is an amplitude of the precession motion of the spin on the ith sublattice. The equations for the spin on the sublattice 5–8 are given by following replacements for Eqs. (A2)–(A5): $\Delta S_1 \leftrightarrow \Delta S_5$, $\Delta S_2 \leftrightarrow \Delta S_6$, $\Delta S_3 \leftrightarrow \Delta S_7$, $\Delta S_4 \leftrightarrow \Delta S_8$, and $S \rightarrow -S$.

By solving the secular equation for ΔS_1–ΔS_8 obtained from the above equations, we can derive the the spin wave frequencies.

APPENDIX B

The theoretical ESR resonance energies in the 1/2-plateau phase with a 16-sublattice spin structure are derived from a classical spin wave calculation. These energies correspond to the absolute values of the eigenvalues for the following matrices $\tilde{\boldsymbol{M}}$:

$$\tilde{\boldsymbol{M}} = \begin{pmatrix}
-Q & -A & -B & -B & -D & 0 & -B & 0 & 0 & 0 & -D & -A & -D & -B & 0 & 0\\
A & -P & A & A & 0 & D & 0 & A & D & A & 0 & 0 & A & D & 0 & 0\\
-B & -A & -Q & -B & -A & 0 & -D & 0 & -B & -D & 0 & 0 & 0 & 0 & -D & -B\\
-B & -A & -B & -Q & 0 & -B & 0 & -D & 0 & 0 & -B & -D & 0 & 0 & -A & -D\\
D & 0 & A & 0 & -P & A & A & A & A & 0 & D & 0 & D & 0 & 0 & A\\
0 & -D & 0 & -B & -A & -Q & -B & -B & -D & 0 & -B & 0 & 0 & -D & -A & 0\\
-B & 0 & -D & 0 & -A & -B & -Q & -B & 0 & -D & 0 & -A & 0 & -B & -D & 0\\
0 & -A & 0 & -D & -A & -B & -B & -Q & 0 & -B & 0 & -D & -B & 0 & 0 & -D\\
0 & -D & -B & 0 & -A & -D & 0 & 0 & -Q & -B & -B & -A & 0 & -D & 0 & -B\\
0 & -A & -D & 0 & 0 & 0 & -D & -B & -B & -Q & -B & -A & -B & 0 & -D & 0\\
-D & 0 & 0 & -B & -D & -B & 0 & 0 & -B & -B & -Q & -A & -D & 0 & -A & 0\\
A & 0 & 0 & D & 0 & 0 & A & D & A & A & A & -P & 0 & A & 0 & D\\
-D & -A & 0 & 0 & -D & 0 & 0 & -B & 0 & -B & -D & 0 & -Q & -B & -A & -B\\
-B & -D & 0 & 0 & 0 & -D & -B & 0 & -D & 0 & 0 & -A & -B & -Q & -A & -B\\
0 & 0 & D & A & 0 & A & D & 0 & 0 & D & A & 0 & A & A & -P & A\\
0 & 0 & -B & -D & -A & 0 & 0 & -D & -B & 0 & 0 & -D & -B & -B & -A & -Q
\end{pmatrix}, \tag{B1}$$

$$A = (J_1 S - g\mu_B H)S, \tag{B2}$$

$$B = J_2 S, \tag{B3}$$

$$D = 2J_3 S, \tag{B4}$$

$$P = -3J_1 S - 3J_3 S + g\mu_B H S, \tag{B5}$$

$$Q = J_1 S - 2J_2 S - J_3 S + g\mu_B H S. \tag{B6}$$

APPENDIX C

According to the magnetoelastic theory proposed by Penc *et al.* [16,28], a model Hamiltonian for a single tetrahedron embedded on the pyrochlore lattice is given as

$$\begin{aligned}\mathcal{H}'_{\mathrm{ME}} = {} & 2\sqrt{6}J\Lambda_{A_1} - 4HM - 2J \\ & \times \left(\alpha_{A_1}\Lambda_{A_1}\rho_{A_1} + \alpha_E \boldsymbol{\Lambda}_E \cdot \boldsymbol{\rho}_E + \alpha_{T_2}\boldsymbol{\Lambda}_{T_2}\cdot\boldsymbol{\rho}_{T_2}\right) \\ & + \left(K_{A_1}\rho_{A_1}^2 + K_E{\boldsymbol{\rho}_E}^2 + K_{T_2}{\boldsymbol{\rho}_{T_2}}^2\right). \end{aligned} \tag{C1}$$

Here, J is the exchange constant when the system has no spin correlation, α_R is the strength of the spin-lattice coupling, ρ_R is the amplitude of the distortion, and K_R is the elastic coupling constant for R ($R = A_1$, E or T_2) mode. Λ_R's are expressed as [16,28]

$$\begin{pmatrix}\Lambda_{A_1}\\ \Lambda_{E,1}\\ \Lambda_{E,2}\\ \Lambda_{T_2,1}\\ \Lambda_{T_2,2}\\ \Lambda_{T_2,3}\end{pmatrix} = \begin{pmatrix} \frac{1}{\sqrt{6}} & \frac{1}{\sqrt{6}} & \frac{1}{\sqrt{6}} & \frac{1}{\sqrt{6}} & \frac{1}{\sqrt{6}} & \frac{1}{\sqrt{6}} \\ \frac{1}{\sqrt{3}} & \frac{-1}{2\sqrt{3}} & \frac{-1}{2\sqrt{3}} & \frac{-1}{2\sqrt{3}} & \frac{-1}{2\sqrt{3}} & \frac{1}{\sqrt{3}} \\ 0 & \frac{1}{2} & \frac{-1}{2} & \frac{-1}{2} & \frac{1}{2} & 0 \\ 0 & 0 & \frac{-1}{\sqrt{2}} & \frac{1}{\sqrt{2}} & 0 & 0 \\ 0 & \frac{-1}{\sqrt{2}} & 0 & 0 & \frac{1}{\sqrt{2}} & 0 \\ \frac{-1}{\sqrt{2}} & 0 & 0 & 0 & 0 & \frac{1}{\sqrt{2}} \end{pmatrix} \begin{pmatrix} \boldsymbol{S}_1\cdot\boldsymbol{S}_2 \\ \boldsymbol{S}_1\cdot\boldsymbol{S}_3 \\ \boldsymbol{S}_1\cdot\boldsymbol{S}_4 \\ \boldsymbol{S}_2\cdot\boldsymbol{S}_3 \\ \boldsymbol{S}_2\cdot\boldsymbol{S}_4 \\ \boldsymbol{S}_3\cdot\boldsymbol{S}_4 \end{pmatrix}, \tag{C2}$$

where $\boldsymbol{S}_i$ (i = 1–4) is a spin on a vertex of the tetrahedron. From the equilibrium conditions $\partial\mathcal{H}'_{\mathrm{ME}}/\partial\rho_{\mathrm{R}} = 0$, the energy minima are given by following equation:

$$\rho_R = (\alpha_R J/K_R)\Lambda_R. \tag{C3}$$

By substituting this equation into Eq. (C1), an effective Hamiltonian [16,28], given as Eq. (1), and the exchange interactions [42], given as Eqs. (3)–(8), are derived.

[1] J. Villain, Z. Phys. B **33**, 31 (1979).
[2] R. Moessner and J. T. Chalker, Phys. Rev. B **58**, 12049 (1998).
[3] B. Canals and C. Lacroix, Phys. Rev. B **61**, 1149 (2000).
[4] Y. Kino and B. Luthi, Solid State Commun. **9**, 805 (1971).
[5] R. Plumier, M. Lecommte, and M. Sougi, J. Phys. Lett. **38**, 149 (1977).
[6] M. T. Rovers, P. P. Kyriakou, H. A. Dabkowska, G. M. Luke, M. I. Larkin, and A. T. Savici, Phys. Rev. B **66**, 174434 (2002).
[7] S.-H. Lee, C. Broholm, T. H. Kim, W. Ratcliff, and S.-W. Cheong, Phys. Rev. Lett. **84**, 3718 (2000).
[8] Y. Yamashita and K. Ueda, Phys. Rev. Lett. **85**, 4960 (2000).
[9] O. Tchernyshyov, R. Moessner, and S. L. Sondhi, Phys. Rev. Lett. **88**, 067203 (2002).
[10] O. Tchernyshyov, R. Moessner, and S. L. Sondhi, Phys. Rev. B **66**, 064403 (2002).
[11] N. Terada, S. Mitsuda, H. Ohsumi, and K. Tajima, J. Phys. Soc. Jpn. **75**, 023602 (2006).
[12] F. Ye, Y. Ren, Q. Huang, J. A. Fernandez-Baca, P. Dai, J. W. Lynn, and T. Kimura, Phys. Rev. B **73**, 220404(R) (2006).
[13] F. Damay, M. Poienar, C. Martin, A. Maignan, J. Rodriguez-Carvajal, G. André, and J. P. Doumerc, Phys. Rev. B **80**, 094410 (2009).
[14] A. Zorko, O. Adamopoulos, M. Komelj, D. Arčon, and A. Lappas, Nat. Commun. **5**, 3222 (2014).
[15] A. Zorko, J. Komelj, M. Komelj, O. Adamopoulos, H. Luetkens, D. Arčon, and A. Lappas, Sci. Rep. **5**, 9272 (2015).
[16] K. Penc, N. Shannon, and H. Shiba, Phys. Rev. Lett. **93**, 197203 (2004).
[17] H. Ueda, H. A. Katori, H. Mitamura, T. Goto, and H. Takagi, Phys. Rev. Lett. **94**, 047202 (2005).
[18] H. Ueda, H. Mitamura, T. Goto, and Y. Ueda, Phys. Rev. B **73**, 094415 (2006).
[19] H. Mitamura, H. Ueda, H. A. Katori, S. Takeyama, T. Sakakibara, Y. Ueda, and H. Takagi, J. Phys. Soc. Jpn. **76**, 085001 (2007).
[20] E. Kojima, A. Miyata, S. Miyabe, S. Takeyama, H. Ueda, and Y. Ueda, Phys. Rev. B **77**, 212408 (2008).
[21] A. Miyata, H. Ueda, Y. Ueda, Y. Motome, N. Shannon, K. Penc, and S. Takeyama, J. Phys. Soc. Jpn. **80**, 074709 (2011).
[22] A. Miyata, H. Ueda, Y. Ueda, H. Sawabe, and S. Takeyama, Phys. Rev. Lett. **107**, 207203 (2011).
[23] A. Miyata, H. Ueda, Y. Ueda, Y. Motome, N. Shannon, K. Penc, and S. Takeyama, J. Phys. Soc. Jpn. **81**, 114701 (2012).
[24] A. Miyata, S. Takeyama, and H. Ueda, Phys. Rev. B **87**, 214424 (2013).
[25] A. Miyata, H. Ueda, and S. Takeyama, J. Phys. Soc. Jpn. **83**, 063702 (2014).
[26] M. Matsuda, H. Ueda, A. Kikkawa, Y. Tanaka, K. Katsumata, Y. Narumi, T. Inami, Y. Ueda, and S.-H. Lee, Nat. Phys. **3**, 397 (2007).
[27] M. Matsuda, K. Ohoyama, S. Yoshii, H. Nojiri, P. Frings, F. Duc, B. Vignolle, G. L. J. A. Rikken, L.-P. Regnault, S.-H. Lee, H. Ueda, and Y. Ueda, Phys. Rev. Lett. **104**, 047201 (2010).
[28] K. Penc, N. Shanon, Y. Motome, and H. Shiba, J. Phys.: Condens. Matter **19**, 145267 (2007).
[29] D. L. Bergman, R. Shindou, G. A. Fiete, and L. Balents, Phys. Rev. B **74**, 134409 (2006).
[30] Y. Motome, K. Penc, and N. Shannon, J. Magn. Magn. Mater. **300**, 57 (2006).
[31] S. Kimura, M. Hagiwara, T. Takeuchi, H. Yamaguchi, H. Ueda, Y. Ueda, and K. Kindo, Phys. Rev. B **83**, 214401 (2011).
[32] J.-H. Chung, M. Matsuda, S.-H. Lee, K. Kakurai, H. Ueda, T. J. Sato, H. Takagi, K.-P. Hong, and S. Park, Phys. Rev. Lett. **95**, 247204 (2005).
[33] S. Kimura, M. Hagiwara, H. Ueda, Y. Narumi, K. Kindo, H. Yashiro, T. Kashiwagi, and H. Takagi, Phys. Rev. Lett. **97**, 257202 (2006).
[34] G.-W. Chern, C. J. Fennie, and O. Tchernyshyov, Phys. Rev. B **74**, 060405 (2006).
[35] E. Choi, G.-W. Chern, and N. B. Perkins, Phys. Rev. B **87**, 054418 (2013).
[36] A. N. Yaresko, Phys. Rev. B **77**, 115106 (2008).
[37] Y. Sawada, S. Kimura, K. Watanabe, and H. Ueda, J. Phys. Conf. Ser. **568**, 042028 (2014).

[38] T. Arima, J. Phys. Soc. Jpn. **76**, 073702 (2007).
[39] S. Miyahara and N. Furukawa, J. Phys. Soc. Jpn. **80**, 073708 (2011).
[40] K. Penc, J. Romhányi, T. Rõõm, U. Nagel, Á. Antal, T. Fehér, A. Jánossy, H. Engelkamp, H. Murakawa, Y. Tokura, D. Szaller, S. Bordács, and I. Kézsmárki, Phys. Rev. Lett. **108**, 257203 (2012).
[41] I. Kèzsmarkì, N. Kida, H. Murakawa, S. Bordàcs, Y. Onose, and Y. Tokura, Phys. Rev. Lett. **106**, 057403 (2011).
[42] S. Kimura, M. Hagiwara, T. Takeuchi, H. Yamaguchi, and K. Kindo, J. Phys. Soc. Jpn. **83**, 113709 (2014).
[43] D. Nakamura, A. Miyata, Y. Aida, H. Ueda, and S. Takeyama, J. Phys. Soc. Jpn. **83**, 113703 (2014).
[44] S. Zherlitsyn, V. Tsurkan, A. A. Zvyagin, S. Yasin, S. Erfanifam, R. Beyer, M. Naumann, E. Green, J. Wosnitza, and A. Loidl, Phys. Rev. B **91**, 060406(R) (2015).
[45] A. V. Chubukov, Phys. Rev. B **44**, 4693 (1991).
[46] N. Shannon, T. Momoi, and P. Sindzingre, Phys. Rev. Lett. **96**, 027213 (2006).
[47] T. Momoi, P. Sindzingre, and N. Shannon, Phys. Rev. Lett. **97**, 257204 (2006).
[48] M. E. Zhitomirsky and H. Tsunetsugu, Europhys. Lett. **92**, 37001 (2010).
[49] L. E. Svistov, T. Fujita, H. Yamaguchi, S. Kimura, K. Omura, A. Prokofiev, A. I. Smilnov, Z. Honda, and M. Hagiwara, JETP Lett. **93**, 21 (2011).